ELSEVIER

An improved SPH method: Towards higher order convergence

G. Oger *, M. Doring, B. Alessandrini, P. Ferrant

Fluid Mechanics Laboratory (CNRS UMR6598), Ecole Centrale de Nantes, 44321 Nantes, France

Abstract

This paper evaluates various formulations of the SPH method for solving the Euler equations. Convergence and stability aspects are discussed and tested, taking into account subtleties induced by the presence of a free surface. The coherence between continuity and momentum equations is considered using a variational study. The use of renormalization to improve the accuracy of the simulations is investigated and discussed. A new renormalization-based formulation involving wide accuracy improvements of the scheme is introduced. The classical SPH and renormalized approaches are compared to the new method using simple test cases, thus outlining the efficiency of this new improved SPH method. Finally, the so-called "tensile instability" is shown to be prevented by this enhanced SPH method, through accuracy increases in the gradient approximations.
© 2007 Elsevier Inc. All rights reserved.

Keywords: Renormalization; SPH convergence; Free surface considerations; New SPH formulation

1. Introduction

Smoothed particle hydrodynamics (SPH) is a promising tool for hydrodynamic applications as it is simple, efficient and robust [1,2]. This easy-to-code meshless method easily handles complex free surface flow problems displaying strong non-linearities, including breaking waves. SPH has a wide range of applications in mechanical engineering topics [3–5] where strong non-linearities occur, as well as coupled fluid/structure interaction problems [6]. This method is based on the convolution of variables through a kernel (or its gradient) to estimate the velocity and pressure gradients. This convolution theoretically ensures second order accuracy for the continuous approach. However, the discretized convolution approximations are insufficiently accurate for obtaining pressure and velocity fields regular enough to exploit fully. Integrals are approximated using a trapeze-like quadrature formula. In order to limit the computational costs, only a few points are used, thus compromising the accuracy. In this paper, particular attention is first paid to the quantification of errors in the gradient approximation procedures using kernel gradients on a set of unstructured interpolation points. Then

---

* Corresponding author.
 E-mail address: guillaume.oger@ec-nantes.fr (G. Oger).

various aspects related to the global Euler equation discretization, namely the coherence of the SPH method, the reciprocity principle and free surface conditions, are discussed. Some kernel corrective terms for improving the accuracy of gradient estimations on a set of interpolation points [7–9] are available. The main difficulty however then consists of implementing these tools in the SPH scheme. In this paper, the kernel correction term we use is the so-called ''renormalization'' first introduced by Johnson and Beissel [10], and adapted by Randles and Libersky [11] (see also [8,9]). We then consider how accuracy requirements conflict with coherence, the reciprocity principle and free surface considerations. Arising from this discussion, an improved SPH method based on renormalization and displaying strong convergence properties is introduced and justified. An original procedure for detecting the free surface is adopted, enabling this new scheme to operate in the presence of a free boundary. Stability and accuracy aspects of this methodology, including artificial viscosity [12,13], are then discussed. Finally, this new formulation is validated through various test cases.

2. Analysis of the gradient interpolation of a field f

The classical SPH method is based on gradient approximations, which are achieved by convolving the variables with a kernel function W, applying

$$\langle \nabla f(\vec{x}) \rangle = \int_D f(\vec{x}^*) \nabla W(\vec{x} - \vec{x}^*) \, d\vec{x}^* \tag{1}$$

with $\vec{x} = (x, y)$ and $\vec{x}^* = (x^*, y^*)$ in Cartesian coordinate system.

The kernel function W used throughout this paper is a cubic B-spline [12] for which the compact support D is a radius $2h$, where the smoothing length h acts as a space discretization agent.

Starting from a second order Taylor expansion

$$f(\vec{x}^*) = f(\vec{x}) + (x^* - x)\frac{\partial f(\vec{x})}{\partial x} + (y^* - y)\frac{\partial f(\vec{x})}{\partial y} + O(h^2),$$

it is possible to determine the accuracy of (1) by convolving $f(\vec{x}^*)$ with the kernel gradient, giving

$$\int_D f(\vec{x}^*) \nabla W \, d\vec{x}^* = f(\vec{x}) \underbrace{\int_D \nabla W \, d\vec{x}^*}_{A} + \frac{\partial f(\vec{x})}{\partial x} \underbrace{\int_D (x^* - x) \nabla W \, d\vec{x}^*}_{B} + \frac{\partial f(\vec{x})}{\partial y} \underbrace{\int_D (y^* - y) \nabla W \, d\vec{x}^*}_{C} + O(h^2),$$

where for brevity, ∇W denotes $\nabla W(\vec{x} - \vec{x}^*)$.

Here, integrals A, B and C are respectively $\begin{pmatrix} 0 \\ 0 \end{pmatrix}$, $\begin{pmatrix} 1 \\ 0 \end{pmatrix}$ and $\begin{pmatrix} 0 \\ 1 \end{pmatrix}$.

Consequently, this continuous convolution is equivalent to the Taylor expansion and is thus accurate to the second order. Note that this two-dimensional approach can be extended to the more generalized three-dimensional context.

2.1. Discrete approximation

When implemented, the SPH scheme uses a set of interpolation points to discretize the fluid volume. Each of these points carries discrete values of the calculated fields and intrinsic data such as volume. The volume is important since it acts as a weight term for the discrete approximation of the previous integrals. Indeed, calling ω_i the volume carried by a given point i, the continuous equation (1) is approximated by

$$\langle \nabla f(\vec{x}) \rangle = \sum_{i=1}^{N} f(\vec{x}_i) \nabla W(\vec{x} - \vec{x}_i) \omega_i, \tag{2}$$

where N stands for the number of points within domain D. This last approximation is based on the trapeze-like quadrature formula (3) [9]

$$\int_D g(\vec{x}^*) \, d\vec{x}^* \approx \sum_{i=1}^{N} g(\vec{x}_i) \omega_i. \tag{3}$$

This quadrature formula may result in large problematic errors in the discrete interpolation procedure, since it compromises the accuracy of interpolation (1), which was shown to be $O(h^2)$.

The gradient approximation (2) does not systematically respect the following equalities:

$$\sum_{i=1}^{N} \nabla W(\vec{x} - \vec{x}_i)\omega_i = \vec{0}, \tag{4}$$

$$\sum_{i=1}^{N} (x_i - x) \nabla W(\vec{x} - \vec{x}_i)\omega_i = \begin{pmatrix} 1 \\ 0 \end{pmatrix}, \tag{5}$$

$$\sum_{i=1}^{N} (y_i - y) \nabla W(\vec{x} - \vec{x}_i)\omega_i = \begin{pmatrix} 0 \\ 1 \end{pmatrix}, \tag{6}$$

since for computational time saving reasons only a few points contribute to this quadrature. Conditions (4)–(6) can only be met using a set of equidistant interpolation points on a Cartesian grid. Although we can initialize any simulation with data points along a Cartesian grid, the subsequent fluid flow results in a disordered distribution of points.

Note that approximation (3) tends towards a strict equality only as the number N of points used in the quadrature tends towards infinity. Taking h as a specific scale of domain D, and calling Δx a specific distance
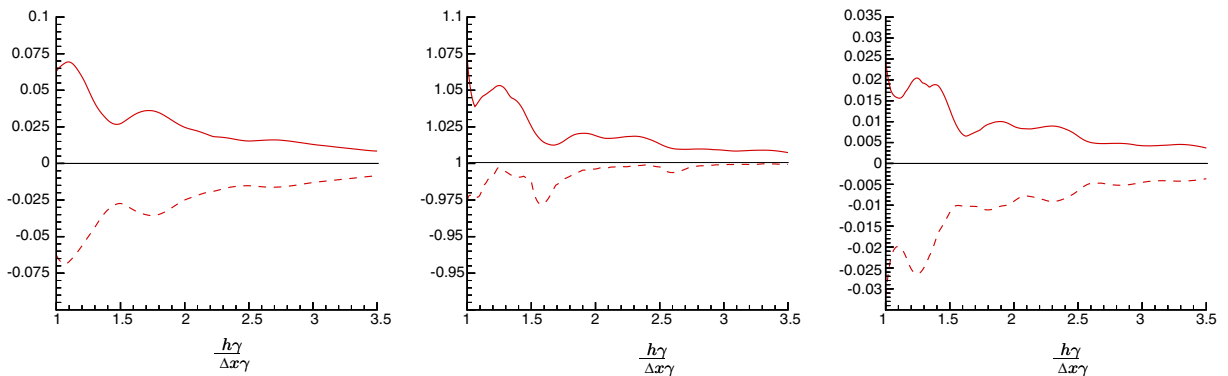

Fig. 1. Results obtained for the convergence of the $\vec{x}$ component of $\sum \nabla W(\vec{x}^* - \vec{x}_i)\omega_i$, $\sum (x^* - x_i)\nabla W(\vec{x}^* - \vec{x}_i)\omega_i$ and $\sum (y^* - y_i)\nabla W(\vec{x}^* - \vec{x}_i)\omega_i$ (from left to right, respectively); for a sample of 500 points: (—) max, (- - -) min.
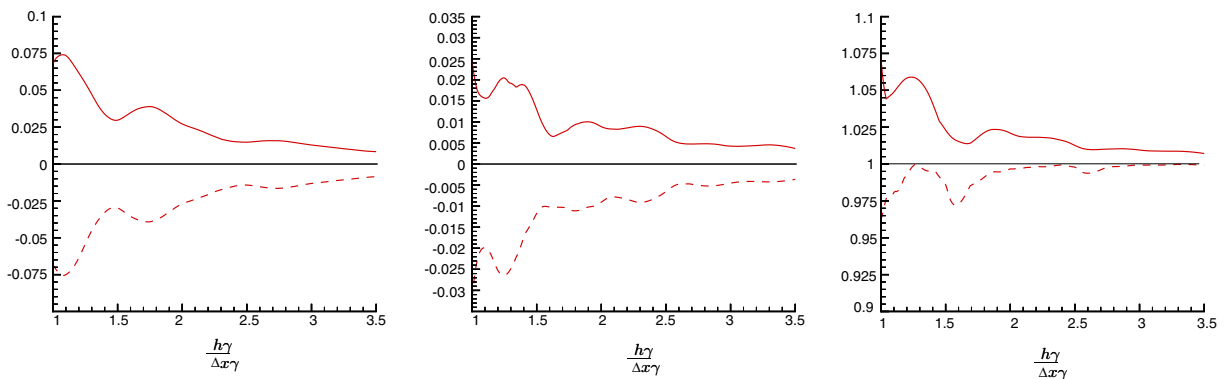

Fig. 2. Results obtained for the convergence of the $\vec{y}$ component of approximations $\sum \nabla W(\vec{x}^* - \vec{x}_i)\omega_i$, $\sum (x^* - x_i)\nabla W(\vec{x}^* - \vec{x}_i)\omega_i$ and $\sum (y^* - y_i)\nabla W(\vec{x}^* - \vec{x}_i)\omega_i$ (from left to right, respectively); for a sample of 500 points: (—) max, (- - -) min.

between two points, the condition to be respected is $\frac{h}{\Delta x} \to \infty$, this convergence condition being added to $h \to 0$, which is related to the kernel-based approximation [9].

To demonstrate how the spacing of interpolation points can affect convergence, some test results are presented in Figs. 1 and 2. These figures show the errors occurring in the approximation of conditions (4)–(6) plotted against $\frac{h}{\Delta x}$. For these tests achieved on arbitrarily spaced point distributions with an imposed smoothing length (only Δx varies), care was taken with the determination of the discrete volumes ω_i, to ensure there were no voids between the interpolation points.

These two figures illustrate that the errors in gradient approximations are non-negligible unless we use a high value of $\frac{h}{\Delta x}$. For example, $\frac{h}{\Delta x} = 3$ corresponds to a contribution of about 130 interpolation points within the kernel compact support for a two-dimensional problem, inducing high computational costs. This fact is the main motivation for applying some corrective terms on the kernel gradient, since practically, an acceptable value for $\frac{h}{\Delta x}$ must be in the range of 1.2–1.5.

3. Euler equations

In order to achieve symmetry and to provide some reciprocity properties, both the continuity and the momentum conservation equations must be first transformed [12] before their discretization:

$$\frac{\vec{\nabla}P}{\rho} = \frac{P}{\rho^\sigma}\vec{\nabla}\left(\frac{1}{\rho^{1-\sigma}}\right) + \rho^{\sigma-2}\vec{\nabla}\left(\frac{P}{\rho^{\sigma-1}}\right), \tag{7}$$

$$\rho\vec{\nabla}\vec{v} = \frac{\vec{\nabla}(\rho^{\sigma-1}\vec{v}) - \vec{v}\vec{\nabla}\rho^{\sigma-1}}{\rho^{\sigma-2}}, \tag{8}$$

where P, $\vec{v}$ and ρ stand for the pressure, the velocity and the density, respectively.

As these equations are valid for any value of an arbitrary parameter $\sigma \in \mathbb{R}$, assuming $\rho > 0 \in \mathbb{R}^d \times \mathbb{R}^+$, the possibilities for such a transformation are infinite.

We deduce from Eqs. (7) and (8) the following system for the discretized form of the Euler equations:

$$\frac{\mathrm{d}\vec{x}_i}{\mathrm{d}t} = \vec{v}_i, \tag{9}$$

$$\frac{\mathrm{d}\rho_i}{\mathrm{d}t} = \sum_j m_j\left(\frac{\vec{v}_i - \vec{v}_j}{\rho_i^{\sigma-2}\rho_j^{2-\sigma}}\right)\nabla W(\vec{x}_i - \vec{x}_j), \tag{10}$$

$$\frac{\mathrm{d}\vec{v}_i}{\mathrm{d}t} = \vec{g} - \sum_j m_j\left(\frac{P_i}{\rho_i^\sigma\rho_j^{2-\sigma}} + \frac{P_j}{\rho_i^{2-\sigma}\rho_j^\sigma}\right)\nabla W(\vec{x}_i - \vec{x}_j), \tag{11}$$

where any interpolation point i can be seen as a material particle carrying a mass $m_i = \rho_i\omega_i$, which does not vary in time [9,2].

In order to allow the above system of equations to be closed, the Tait's equation of state (12) is used

$$P(\rho) = \frac{\rho_0 c_0^2}{\gamma}\left[\left(\frac{\rho}{\rho_0}\right)^\gamma - 1\right], \tag{12}$$

where c_0, ρ_0 and γ are the nominal speed of sound, the nominal fluid density and the polytropic constant, respectively. Note that $\gamma = 7$ is usually retained for water simulations, while the nominal speed of sound c_0 is chosen arbitrarily in respect of a low Mach number ($Ma < 0.1$) to ensure low compressibility effects (responsible for the pseudo-compressible feature of SPH method [12]).

3.1. SPH scheme coherence

The symmetry in the equations, as discussed above, allows a more sophisticated interpretation of the SPH scheme. Indeed, various investigations by Bonet and Lok [8] and Vila [9] lead to the conclusion that once

discretized, the continuity and the momentum conservation equations could be closely linked, inducing the need for coherence within the scheme. This coherence is usually referred to as "consistency" in the literature (see [8]), but this usually relates to numerical convergence aspects in CFD. In order to avoid any ambiguity, we prefer here the term "coherence". This coherence formally implies a link between the form of the momentum equation, and the choice made for the continuity equation discretization.

Generalizing the variational study introduced by Bonet et al., we start from discretization (10) for the continuity equation. Taking a set of N interpolation points used to discretize the fluid domain, the variation of the total stored potential energy within a virtual velocity field $\delta\vec{v}$ applied to these points is

$$D\Pi[\delta\vec{v}] = \sum_{i=1}^{N} \vec{T}_i \cdot \delta\vec{v}_i, \tag{13}$$

where $\vec{T}_i = m_i \frac{d\vec{v}_i}{dt}$ is the force acting on point i. Thus it can be seen that (13) is closely related to the momentum equation.

Unlike Bonet et al., here we define the stress tensor as $\bar{\bar{\sigma}} = -P\bar{\bar{I}}$, since a positive pressure indicates a compression throughout this paper, as is the convention in fluid mechanics.

Eq. (13) may be expanded to

$$D\Pi[\delta\vec{v}] = -\sum_{i=1}^{N} m_i \left(\frac{P_i}{\rho_i^2} \right) D\rho_i[\delta\vec{v}], \tag{14}$$

where $D\rho_i[\delta\vec{v}]$ is clearly related to the continuity equation. Consequently, this last equation demonstrates the direct link between the momentum and the continuity equations.

Using (10) for the continuity equation discretization, we write

$$D\rho_i[\delta\vec{v}] = \sum_{j=1}^{N} m_j \left(\frac{\delta\vec{v}_i - \delta\vec{v}_j}{\rho_i^{\sigma-2}\rho_j^{2-\sigma}} \right) \nabla W(\vec{x}_i - \vec{x}_j). \tag{15}$$

After manipulation, and noting that $\nabla W(\vec{x}_i - \vec{x}_j) = -\nabla W(\vec{x}_j - \vec{x}_i)$, Eq. (15) becomes

$$D\Pi[\delta\vec{v}] = \sum_{i=1}^{N} \left[-\sum_{j=1}^{N} m_i m_j \left(\frac{P_i}{\rho_i^{\sigma}\rho_j^{2-\sigma}} + \frac{P_j}{\rho_i^{2-\sigma}\rho_j^{\sigma}} \right) \nabla W(\vec{x}_i - \vec{x}_j) \right] \cdot \delta\vec{v}_i \tag{16}$$

in which we recognize the discretization (11) of the momentum equation. Note that this link exists even for more complicated problems (see for instance [2]).

In order to ensure coherence, the value of σ used in Eq. (11) must be the same as that used in Eq. (10). Among all the possibilities offered by these equations, two particular symmetrized forms are common in the literature; one for which $\sigma = 2$ adopted by Monaghan [12], and another using $\sigma = 1$, adopted for instance by Vila [9] and Colagrossi and Landrini [14], that is

$$\frac{d\rho_i}{dt} = \rho_i \sum_j \frac{m_j}{\rho_j} (\vec{v}_i - \vec{v}_j) \nabla W(\vec{x}_i - \vec{x}_j), \tag{17}$$

$$\frac{d\vec{v}_i}{dt} = \vec{g} - \sum_j m_j \left(\frac{P_i + P_j}{\rho_i \rho_j} \right) \nabla W(\vec{x}_i - \vec{x}_j). \tag{18}$$

The present study uses these equations, since they are of particular interest. Indeed, for $\sigma = 1$ the term $\nabla\rho$ vanishes from Eqs. (7) and (8), giving

$$\nabla\vec{v} = \nabla\vec{v} - \vec{v}\nabla 1, \tag{19}$$
$$\nabla P = \nabla P + P\nabla 1, \tag{20}$$

where $\nabla 1$ has replaced $\nabla\rho$. This leads to the simplest versions of the equations, allowing high density ratio multiphasic simulations [14], and facilitating the implementation of kernel gradient corrections such as renormalization. Note that $\nabla 1$ is theoretically equal to zero, but is approximated as

$$\langle \nabla 1 \rangle = \sum_j \nabla W(\vec{x}_i - \vec{x}_j) \omega_j$$

in the SPH formalism, as used from now on in the present study.

Note that this term is of major importance in the various analysis and formulations proposed in the present study, since it allows to match the SPH interpolation with Taylor expansion, as discussed further.

3.2. Free surface conditions

The free surface can be seen as the medium abruptly stopping. On this free boundary, the interpolation behaves differently to anywhere else since there is a void within the compact support D where no points are defined.

Navier–Stokes or Euler solvers usually deal with this boundary by imposing kinematic and dynamic conditions. Due to its Lagrangian property, the SPH method implicitly fulfills the kinematic condition. The dynamic condition imposes an appropriate pressure on the free surface. In practice, no additional procedure is implemented in SPH for imposing such a condition. Nevertheless, it is possible to find a specific term in Eq. (18) that acts implicitly as a dynamic condition approximation around the free surface.

The total force acting on a particle i can be written $\vec{F}_i = m_i \frac{d\vec{v}_i}{dt} = \omega_i \rho_i \frac{d\vec{v}_i}{dt}$, which can be expanded to

$$\vec{F}_i = m_i \vec{g} - \omega_i \left[\sum_j P_i \nabla W(\vec{x}_i - \vec{x}_j) \omega_j + \sum_j P_j \nabla W(\vec{x}_i - \vec{x}_j) \omega_j \right]. \tag{21}$$

Written in the continuous case, it can be seen that the above term in square brackets comes from the following convolution:

$$\int_\Omega (P(\vec{x}) + P(\vec{y})) \nabla W(\vec{x} - \vec{y}) \, dV_y,$$

where Ω denotes the volume of the interpolation.

This last term can then be written as

$$\int_\Omega (P(\vec{y}) - P(\vec{x})) \nabla W(\vec{x} - \vec{y}) \, dV_y + \underbrace{2 \int_\Omega P(\vec{x}) \nabla W(\vec{x} - \vec{y}) \, dV_y}_{A}. \tag{22}$$

Here integral A can be seen as an implicit dynamic condition. To illustrate this, consider the example of a droplet in space, that is a fluid volume completely bounded by a free surface. Suppose that no volume forces such as gravity act on it, but a positive and constant pressure P_0 exists everywhere within this volume. This last assumption means that in the absence of integral A, the total force acting on the free surface would be zero. The droplet would thus remain at hydrostatic equilibrium. This example corresponds to the case of an outside pressure equal to P_0. Therefore, as SPH includes the integral A, a positive force exists in the free surface area, making this fluid volume explode under the pressure P_0. This would be the case for a zero outside pressure, as is assumed by SPH. The forces responsible for this expansion are due only to integral A, which involves P_0 itself.

Next we show that integral A is zero everywhere within the fluid volume, except in the area of a free surface. By Green–Ostrogradsky transformation, we obtain

$$2 \int_\Omega P(\vec{x}) \nabla W(\vec{x} - \vec{y}) \, dV_y = 2P(\vec{x}) \int_\Omega \nabla W(\vec{x} - \vec{y}) \, dV_y = -2P(\vec{x}) \int_{\delta\Omega} W(\vec{x} - \vec{y}) \vec{n} \, dS,$$

where $\delta\Omega$ is the edge of Ω, and $\vec{n}$ the local normal to this limit [9].

Consider a point of interest $\vec{x}$ deep within the fluid volume, such that $\delta\Omega$ is not intersected by the free surface. The compact support property of W makes the term $\int_{\delta\Omega} W(\vec{x} - \vec{y}) \vec{n} \, dS$ zero. Likewise, when $\vec{x}$ is placed as illustrated in Fig. 3, we obtain
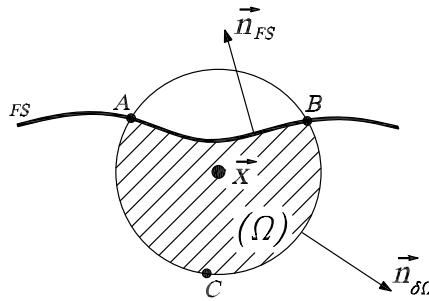
Fig. 3. Case of a point placed in a near free surface area.

$$-2P(\vec{x})\int_{\delta\Omega} W(\vec{x}-\vec{y})\vec{n}\,\mathrm{d}S = -2P(\vec{x})\left[\int_{ACB} W(\vec{x}-\vec{y})\vec{n}_{\delta\Omega}\,\mathrm{d}S + \int_{AB} W(\vec{x}-\vec{y})\vec{n}_{FS}\,\mathrm{d}S\right].$$

Since W is zero on ACB, we see that

$$-2P(\vec{x})\int_{\delta\Omega} W(\vec{x}-\vec{y})\vec{n}\,\mathrm{d}S = -2P(\vec{x})\int_{AB} W(\vec{x}-\vec{y})\vec{n}_{FS}\,\mathrm{d}S. \tag{23}$$

Note this equation's similarity to the pressure integral $-\int_{FS} P\vec{n}\,\mathrm{d}S$, which would be intuitively applied to the free surface as a dynamic condition. It can be seen that this term of force per unit volume, integral A, acts only on the free surface. Furthermore, the orientation of this force follows an approximation to the local normal to the free surface contained in $\int_{AB} W(\vec{x}-\vec{y})\vec{n}_{FS}\,\mathrm{d}S$, and its modulus depends on the distance of $\vec{x}$ from the free surface and the pressure at that point. Due to these properties, integral A acts as a dynamic condition.

The pressure imposed on the free surface comes from within the fluid. This is necessary since the absence of any fluid above the free surface implies a zero external pressure, and thus prevents the direct imposition of external pressure.

The presence of the value 2 in Eq. (22) is due to the approximation by convolution of Eq. (20), and is used in the present study. However, it has to be seen as an approximate dynamic condition coefficient. As some uncertainties remain about this precise value, it could be the subject of further research. For instance, replacing it by an unknown term may help in imposing a more pertinent free surface condition.

Note finally that this coarse dynamic condition approximation is only due to the positive sign in the gradient expression $\nabla P = \nabla P + P\nabla 1$. As a consequence, the absence of any free surface in a fluid problem may allow

$$\nabla P = \nabla P - P\nabla 1 \tag{24}$$

for the momentum equation, as discussed further in this paper.

4. Direct kernel gradient corrective procedure

A wide variety of corrective procedures for improving the accuracy of kernel-based approximations can be found in the literature [7]. In the present study, we focus on the renormalization technique [8–11]. This choice finds its origin in the discrete versions of the Euler equations (17) and (18).

Looking carefully at Eq. (17)

$$\frac{\mathrm{d}\rho_i}{\mathrm{d}t} = \rho_i \sum_j \frac{m_j}{\rho_j}(\vec{v}_i - \vec{v}_j)\nabla W(\vec{x}_i - \vec{x}_j),$$

it can be seen that the velocity gradient is approached using

$$\nabla \vec{v} = \nabla \vec{v} - \vec{v}\nabla 1.$$

This approach can be generalized for any field f by using

$$\nabla f = \nabla f - f \nabla 1. \tag{25}$$

Transforming this Eq. (25) into its continuous convoluted form corresponds to

$$\nabla f(\vec{x})^{\text{SPH}} = \int_D f(\vec{x}^*) \nabla W \, d\vec{x}^* - f(\vec{x}) \int_D \nabla W \, d\vec{x}^*. \tag{26}$$

Recalling the second order Taylor expansion

$$\int_D f(\vec{x}^*) \nabla W \, d\vec{x}^* = f(\vec{x}) \underbrace{\int_D \nabla W \, d\vec{x}^*}_{A} + \frac{\partial f(\vec{x})}{\partial x} \underbrace{\int_D (x^* - x) \nabla W \, d\vec{x}^*}_{B} + \frac{\partial f(\vec{x})}{\partial y} \underbrace{\int_D (y^* - y) \nabla W \, d\vec{x}^*}_{C} + \text{O}(h^2),$$

we find that

$$\nabla f(\vec{x})^{\text{SPH}} = \frac{\partial f(\vec{x})}{\partial x} \underbrace{\int_D (x^* - x) \nabla W \, d\vec{x}^*}_{B} + \frac{\partial f(\vec{x})}{\partial y} \underbrace{\int_D (y^* - y) \nabla W \, d\vec{x}^*}_{C} + \text{O}(h^2). \tag{27}$$

First note that regardless of the accuracy of ∇W, formulation (25) contains the subtraction of $f(\vec{x})$ from $f(\vec{x}^*)$ ensuring that constant fields have zero gradients. This property is of particular interest for the discrete approximation of (26), since it ensures zero gradients for constant fields with any particle distribution, even near the free surface.

In order to ensure exact gradient interpolations of linear fields, we need to ensure that the discrete approximations of B and C are $\begin{pmatrix} 1 \\ 0 \end{pmatrix}$ and $\begin{pmatrix} 0 \\ 1 \end{pmatrix}$, respectively. This is achieved via the renormalization procedure [8–11], which modifies ∇W in the following manner:

$$\sum_{i=1}^{N} (\vec{x}_j - \vec{x}) \otimes \nabla^R W(\vec{x} - \vec{x}_j) \omega_j = \begin{pmatrix} 1 & 0 \\ 0 & 1 \end{pmatrix}.$$

Here $\nabla^R W(\vec{x} - \vec{x}_j)$ stands for $L(\vec{x}) \nabla W(\vec{x} - \vec{x}_j)$, where $L(\vec{x})$ is a (d, d) correction matrix, d being the dimension of the problem. For instance, in the case of a two-dimensional problem, with $d = 2$, we obtain

$$L(\vec{x}) = \begin{pmatrix} \sum_{i=1}^{N} (x_j^1 - x^1) \nabla^1 W(\vec{x} - \vec{x}_j) \omega_j & \sum_{i=1}^{N} (x_j^1 - x^1) \nabla^2 W(\vec{x} - \vec{x}_j) \omega_j \\ \sum_{i=1}^{N} (x_j^2 - x^2) \nabla^1 W(\vec{x} - \vec{x}_j) \omega_j & \sum_{i=1}^{N} (x_j^2 - x^2) \nabla^2 W(\vec{x} - \vec{x}_j) \omega_j \end{pmatrix}^{-1}.$$

This matrix inversion is achievable analytically, thanks to its small size.

We then discretize the continuity equation in the following manner:

$$\frac{d\rho_i}{dt} = \rho_i \sum_j \frac{m_j}{\rho_j} (\vec{v}_i - \vec{v}_j) L(\vec{x}_i) \nabla W(\vec{x}_i - \vec{x}_j). \tag{28}$$

Note that this discretization ensures exact interpolations for both constant and linear fields.

Substituting the variational form of (28) into Eq. (14) leads to the following version of the momentum equation:

$$\frac{d\vec{v}_i}{dt} = \vec{g} - \sum_j \frac{m_j}{\rho_i \rho_j} (P_i L(\vec{x}_i) \nabla W(\vec{x}_i - \vec{x}_j) + P_j L(\vec{x}_j) \nabla W(\vec{x}_i - \vec{x}_j)), \tag{29}$$

which respects the coherence principle previously discussed.

However, this last equation does not provide any guarantee of convergence. Indeed, it is based on

$$\nabla P = \nabla P + P \nabla 1,$$

which does not ensure zero gradients for constant fields since it does not match the Taylor expansion. In addition, the benefits of renormalization are lost because $L(\vec{x}_j)$ in Eq. (29) could adversely affect the interpolation of particle i.

5. Reciprocal interactions and coherence scheme principles relaxation

Looking at Eq. (28), we observe that

$$\omega_i(\operatorname{div}\vec{v})_{j\to i} = \omega_i\frac{m_j}{\rho_j}(\vec{v}_i - \vec{v}_j)L(\vec{x}_i)\nabla W(\vec{x}_i - \vec{x}_j),$$

$$\omega_j(\operatorname{div}\vec{v})_{i\to j} = \omega_j\frac{m_i}{\rho_i}(\vec{v}_j - \vec{v}_i)L(\vec{x}_j)\nabla W(\vec{x}_j - \vec{x}_i).$$

Note that the matrix $L(\vec{x}_i)$ is related to particle i for which we need to evaluate the density time derivative. Furthermore, the components of this matrix depend on the neighborhood space distribution around particle i.

As a consequence, the following inequality appears

$$\omega_i\omega_j(\vec{v}_i - \vec{v}_j)L(\vec{x}_i)\nabla W(\vec{x}_i - \vec{x}_j) \neq \omega_j\omega_i(\vec{v}_j - \vec{v}_i)L(\vec{x}_j)\nabla W(\vec{x}_j - \vec{x}_i)$$

for an irregular particle distribution, since $L(\vec{x}_i) \neq L(\vec{x}_j)$.

As a result, using Eq. (28), we lose the reciprocal interaction property $\omega_j(\operatorname{div}\vec{v})_{i\to j} = \omega_i(\operatorname{div}\vec{v})_{j\to i}$ that was observed in the standard SPH approach, for which $L(\vec{x}_i) = L(\vec{x}_j) = \overline{\overline{I}}$. However, we actually gained accuracy at the expense of the reciprocal interaction principle, due to the renormalization procedure. The increase in simulation quality indicates that the interaction reciprocity is not as important as interpolation accuracy. Conversely, Eq. (29) fulfills the reciprocity principle but negates all the advantages of the renormalization procedure. Note that it is also possible to swap the reciprocal interaction principle for an accuracy improvement on the momentum conservation equation, using

$$\frac{d\vec{v}_i}{dt} = \vec{g} - \sum_j \frac{m_j}{\rho_i\rho_j}(P_i + P_j)L(\vec{x}_i)\nabla W(\vec{x}_i - \vec{x}_j). \tag{30}$$

When used together with Eq. (28), this last equation results in stable simulations of better quality. Unlike Eq. (29), matrix $L(\vec{x}_i)$ (dedicated to particle i) operates without matrix $L(\vec{x}_j)$ in (30). This shows that it is possible for an SPH scheme to flout the coherence principle provided that some accuracy benefits are gained.

6. A new SPH formulation

It has been shown that large improvements in accuracy can be gained by infringing on both the reciprocity and the coherence principles. The last formulation discussed is based on Eqs. (28) and (30). Note that this momentum conservation equation discretization is not the best one since its does not entirely respect the Taylor expansion (27). Constant field gradient will not systematically be zero. Ideally, the following should be applied

$$\nabla P = \nabla P - P\nabla 1$$

to obtain

$$\frac{d\vec{v}_i}{dt} = \vec{g} - \sum_j \frac{m_j}{\rho_i\rho_j}(-P_i + P_j)L(\vec{x}_i)\nabla W(\vec{x}_i - \vec{x}_j)) \tag{31}$$

as advised by Randles and Libersky [11]. This would result in increased accuracy when used jointly with Eq. (28). We shall refer to the system formed by Eqs. (28) and (31) as the ''Taylor-SPH scheme''.

This formulation initially appears to be incorrect because

- It flouts the coherence principle.
- It infringes on the reciprocity principle, to the extent that: $\vec{F}_{i\to j} = \vec{F}_{j\to i}$, where $\vec{F}_{i\to j}$ denotes the force due to particle i on another, j.
- It implies that integral A in (22) is absent, and thus no force is implicitly imposed on the free surface, as it is the case for the original SPH scheme.

However, it was shown earlier that in some conditions the scheme coherence principle can be infringed. A possible justification for the relaxation of the reciprocity principle is to consider particles as interpolated weighted points rather than discrete fluid masses. In fact, only the third point is a real obstacle to this higher order formulation, since there is no longer a dynamic condition approximation.

To illustrate this, and to demonstrate the efficiency of this formulation, a simple validation test case for which no free surface exists is used. This test case involves a two-dimensional weightlessness tank entirely filled with initially calm water with zero internal pressure. This water tank is accelerated following $\vec{\gamma}(t) = \gamma_0 t \cdot \vec{y}$, where γ_0 is an arbitrary constant. Results obtained using the various formulations as discussed are compared in the following sections.

The absence of any free surface allows both the use of our new approach and an exact analytical solution. Considering the above acceleration as a volume force and the tank as static, the Euler equations give the following exact solution for an incompressible fluid:

$$\vec{v}(x, y, t) = \vec{0},$$
$$P(x, y, t) = \rho \gamma_0 y t,$$
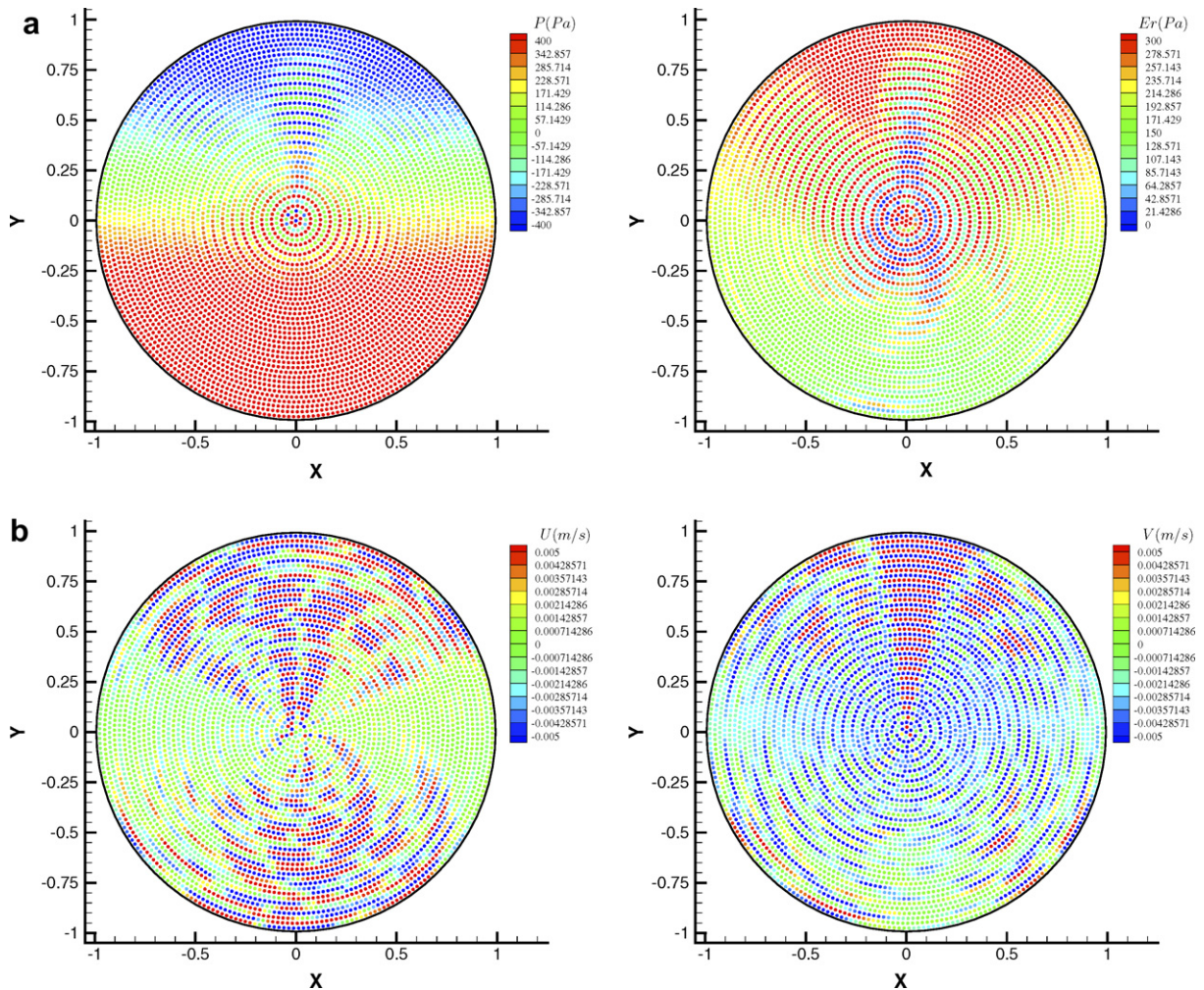
where $\rho = 1000 \text{ kg/m}^3$.

Fig. 4. Standard SPH scheme results. (a) Pressure (left) and error $Er = |P_{\text{SPH}} - P_{\text{exact}}|$ (right). (b) Horizontal (left) and vertical (right) velocity.

Because of the compressibility property of SPH, some differences between the numerical results and the analytical solution would be expected at the beginning of the simulation. For this reason the solutions are compared at $t = 0.102$ s, by which time compressibility effects have disappeared.

In the following simulations a polar distribution of particles displaying no particular symmetry is used. The ratio $\frac{h}{\Delta x} = 1.3$ is adopted and no artificial viscosity is implemented. The arbitrary constant is set to $\gamma_0 = -9.81$ m/s^3 and the nominal speed of sound in the state equation is $c_0 = 80$ m/s. Throughout this paper the solid boundary conditions are imposed using the ghost particle technique.

6.1. Results obtained using the standard coherent SPH scheme

The formulation used here is

$$
\frac{d\rho_i}{dt} = \rho_i \sum_j \frac{m_j}{\rho_j} (\vec{v}_i - \vec{v}_j) \nabla W(\vec{x}_i - \vec{x}_j),
$$
$$
\frac{d\vec{v}_i}{dt} = -\sum_j \frac{m_j}{\rho_i \rho_j} (P_i + P_j) \nabla W(\vec{x}_i - \vec{x}_j).
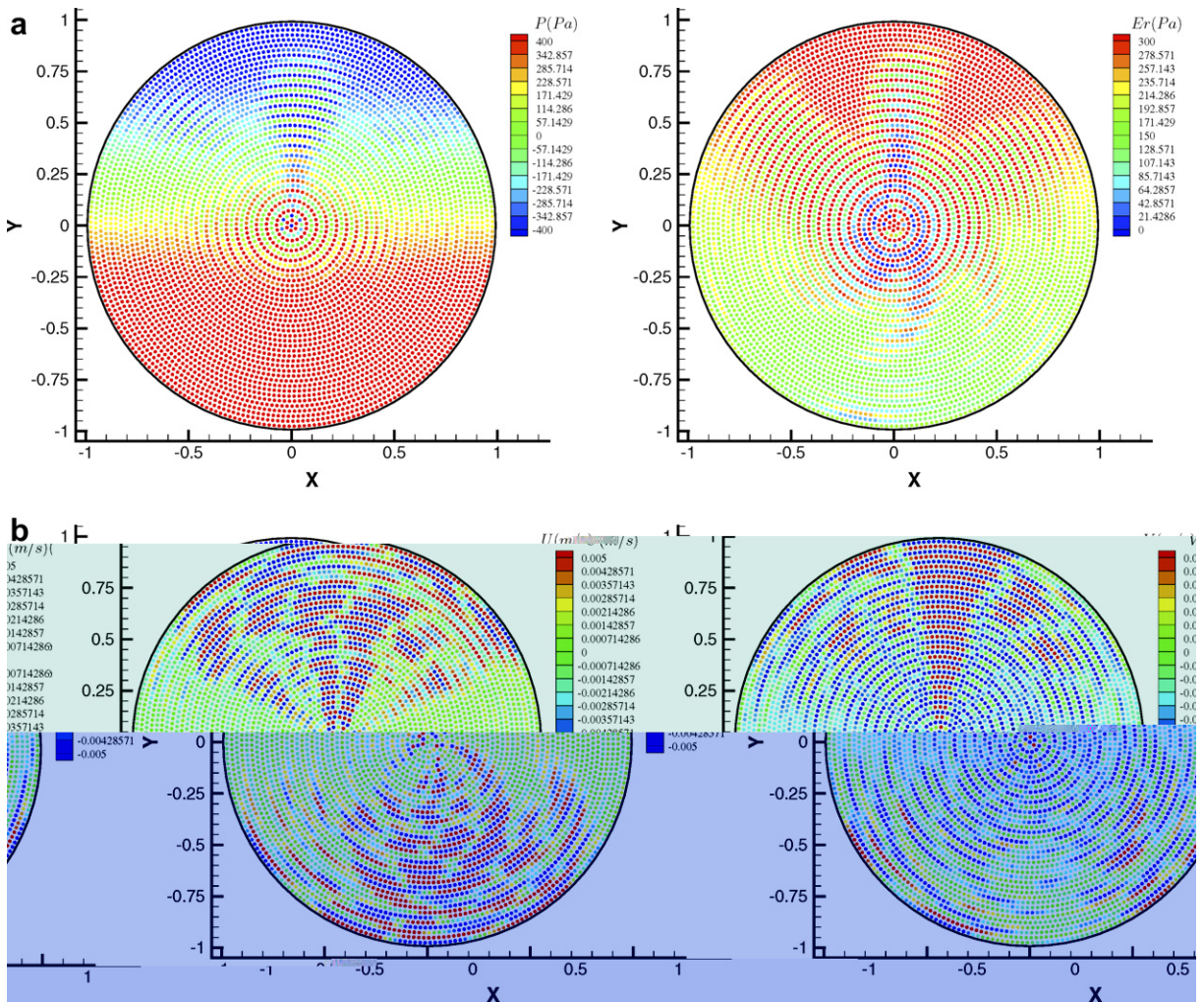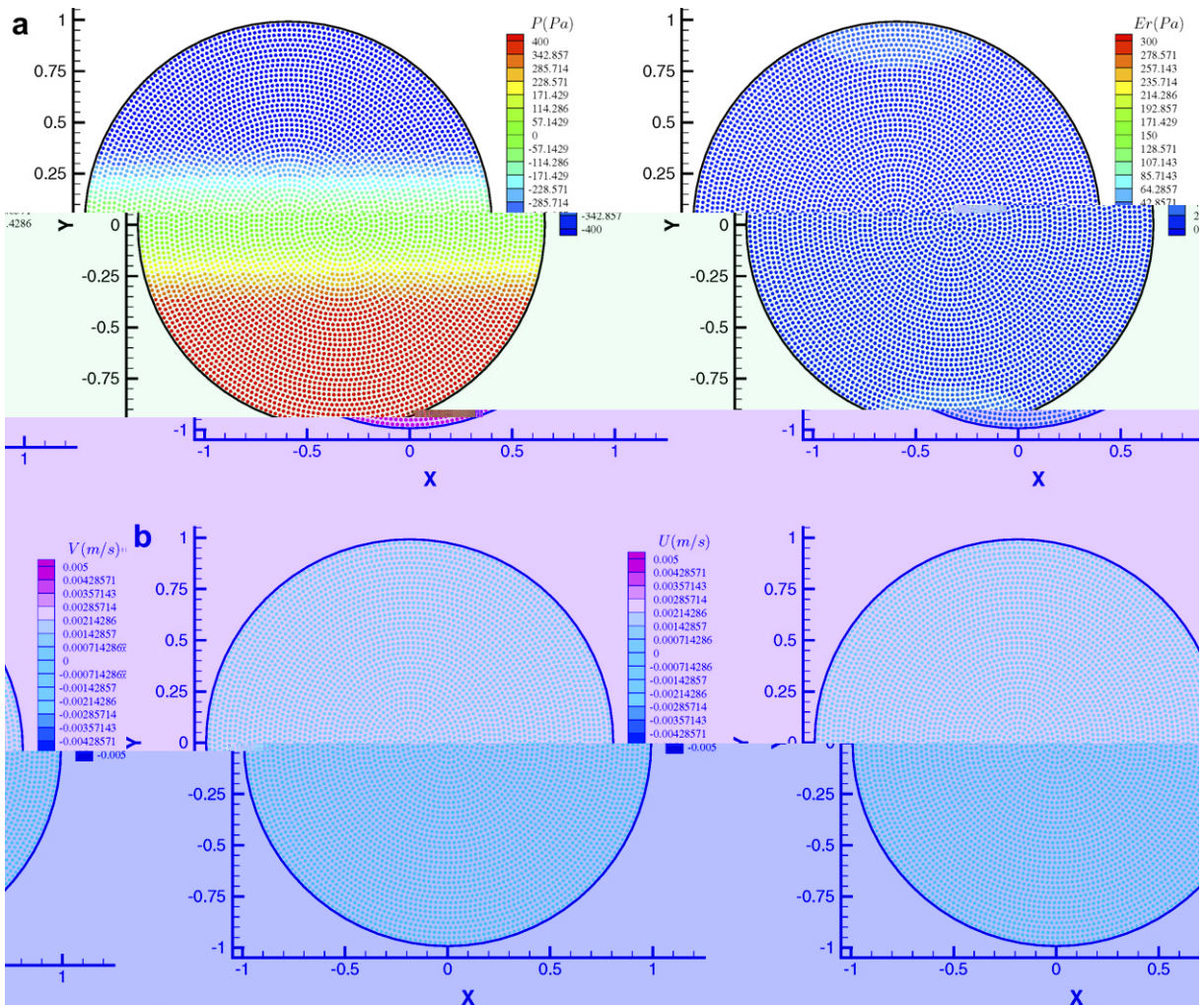$$
(32)

Fig. 5. Non-coherent renormalized SPH scheme results. (a) Pressure (left) and error Er = $|P_{SPH} - P_{exact}|$ (right). (b) Horizontal (left) and vertical (right) velocity.

Fig. 4 emphasizes the poor gradient approximation properties obtained on a particle space distribution different from a Cartesian set with a low value of $\frac{h}{\Delta x}$. The pressure and velocity field results are heterogeneous and show strong errors (100–300% for the pressure) compared to the analytical solution. These crude results obtained for such a simple problem, where smooth regular fields are expected, fully justify the need for corrective terms to increase accuracy.

6.2. Results obtained using a non-coherent renormalized SPH scheme

The Euler equations are discretized here following:

$$
\begin{aligned}
\frac{\mathrm{d}\rho_i}{\mathrm{d}t} &= \rho_i \sum_j \frac{m_j}{\rho_j} (\vec{v}_i - \vec{v}_j) L(\vec{x}_i) \nabla W(\vec{x}_i - \vec{x}_j), \\
\frac{\mathrm{d}\vec{v}_i}{\mathrm{d}t} &= -\sum_j \frac{m_j}{\rho_i \rho_j} (P_i + P_j) L(\vec{x}_i) \nabla W(\vec{x}_i - \vec{x}_j).
\end{aligned}
\tag{33}
$$

Fig. 6. Taylor-SPH scheme results. (a) Pressure (left) and error $Er = |P_{\mathrm{SPH}} - P_{\mathrm{exact}}|$ (right). (b) Horizontal (left) and vertical (right) velocity.

The results obtained using a coherent renormalized SPH scheme were similar, and were omitted for the sake of brevity. Despite the advantages promised by renormalization, the results in Fig. 5 for this non-coherent scheme are similar to those obtained with the standard SPH method (Fig. 4). Here the continuity equation
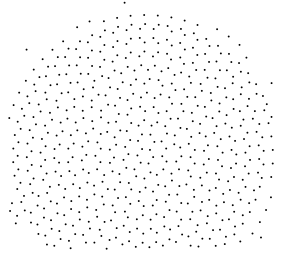
is better discretized than in the standard SPH, but the final result is affected by the discretized form of the momentum equation, which does not respect the Taylor expansion (27).

6.3. Results obtained using the Taylor-SPH scheme

This scheme uses the following form for the Euler equation discretization

$$\frac{d\rho_i}{dt} = \rho_i \sum_j \frac{m_j}{\rho_j} (\vec{v}_i - \vec{v}_j) L(\vec{x}_i) \nabla W(\vec{x}_i - \vec{x}_j),$$

$$\frac{d\vec{v}_i}{dt} = -\sum_j \frac{m_j}{\rho_i \rho_j} (-P_i + P_j) L(\vec{x}_i) \nabla W(\vec{x}_i - \vec{x}_j). \tag{34}$$

As expected from the convergence study previously discussed, this new formulation results in a remarkable increase in accuracy, as Fig. 6 illustrates. The pressure and velocity fields are more regular, closer to the analytical solution and contain fewer errors (maximum 4% for pressure).

6.4. Use of Taylor-SPH on a strongly unstructured particle setting

Next this new SPH scheme is applied to the same test case, but with the heterogeneous particle distribution of Fig. 7.

Because of the strong errors it can produce, this particle distribution is much more penalizing than any particle space distribution naturally induced in a SPH calculation. To make this simulation possible, we use the ratio $\frac{h}{\Delta x} = 1.5$, which corresponds to a mean of 35 neighbors per particle in this two-dimensional test case. Here again, no artificial viscosity is used.

In spite of this strong distribution heterogeneity, the results of Fig. 8 are in good agreement with the analytical solution. Many industrial topics involve complex geometries and use a grid engine to set the initial particle distribution. This new formulation could thus be used with such tools.

7. Extension to free surface flow computations

The accuracy improvement illustrated by the above results is promising. Nevertheless, the Taylor-SPH scheme is not directly applicable in the presence of a free surface. A brutal but efficient solution to this problem is to use the non-coherent renormalized formulation in the free surface area, and the Taylor-SPH scheme
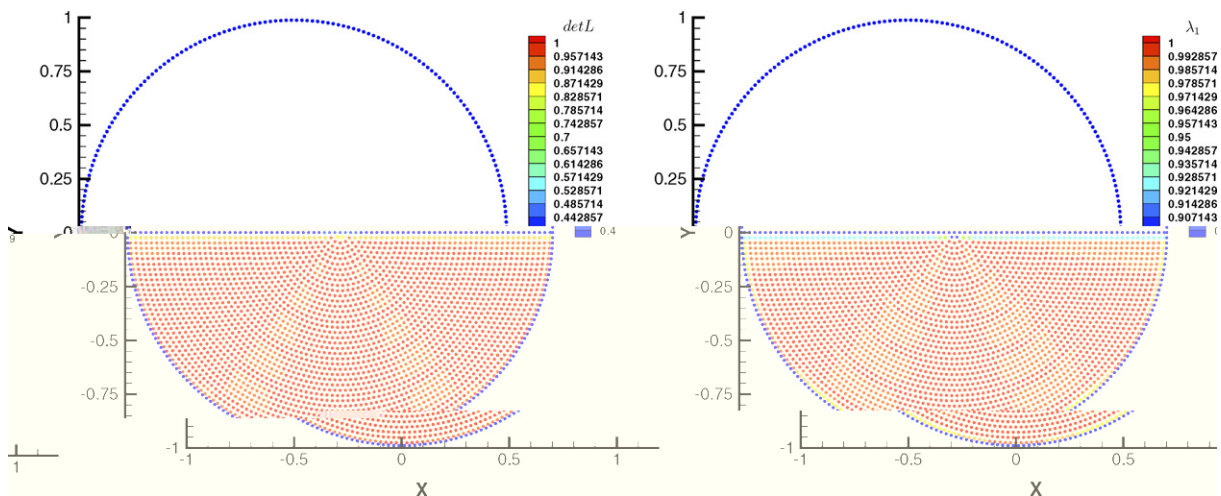

Fig. 9. Determinants (left) and lower eigenvalues (right) of matrix L^{-1}.

everywhere else. This results in a good compromise between accuracy and inclusion of the dynamic free surface condition. The main problem inherent in this technique is to locate the free surface area. Fortunately, the renormalization matrix L itself contains some invaluable indications, since its determinant and lower eigenvalue λ_1 are strongly modified by the absence of weighted points in the kernel support. This absence reveals the presence of a free surface as shown in Fig. 9.

Here we consider features from the L^{-1} matrix since the determinants and eigenvalues of L are more sensitive after inversion.

The lower eigenvalue λ_1 was found to be the best free surface detector. Numerical experiments indicated it was judicious to apply the Taylor-SPH scheme for particles having $\lambda_1 \geqslant 0.97$, and to adopt the non-coherent renormalized scheme for $\lambda_1 < 0.97$. Additionally, to preserve the stability of this hybrid scheme, it is better to also apply this last formulation to particles interacting with those particles having $\lambda_1 < 0.97$. This procedure slightly extends the near free surface area and ensures an increased robustness.

A simple hydrostatic test case of a water tank with a free surface is used as an initial validation of this hybrid scheme. Here again a polar particle distribution is employed, and the free surface is located at $y = 0$. The initial settings of pressure and density need to be the exact compressible solution of this problem [15]. The equations to solve are
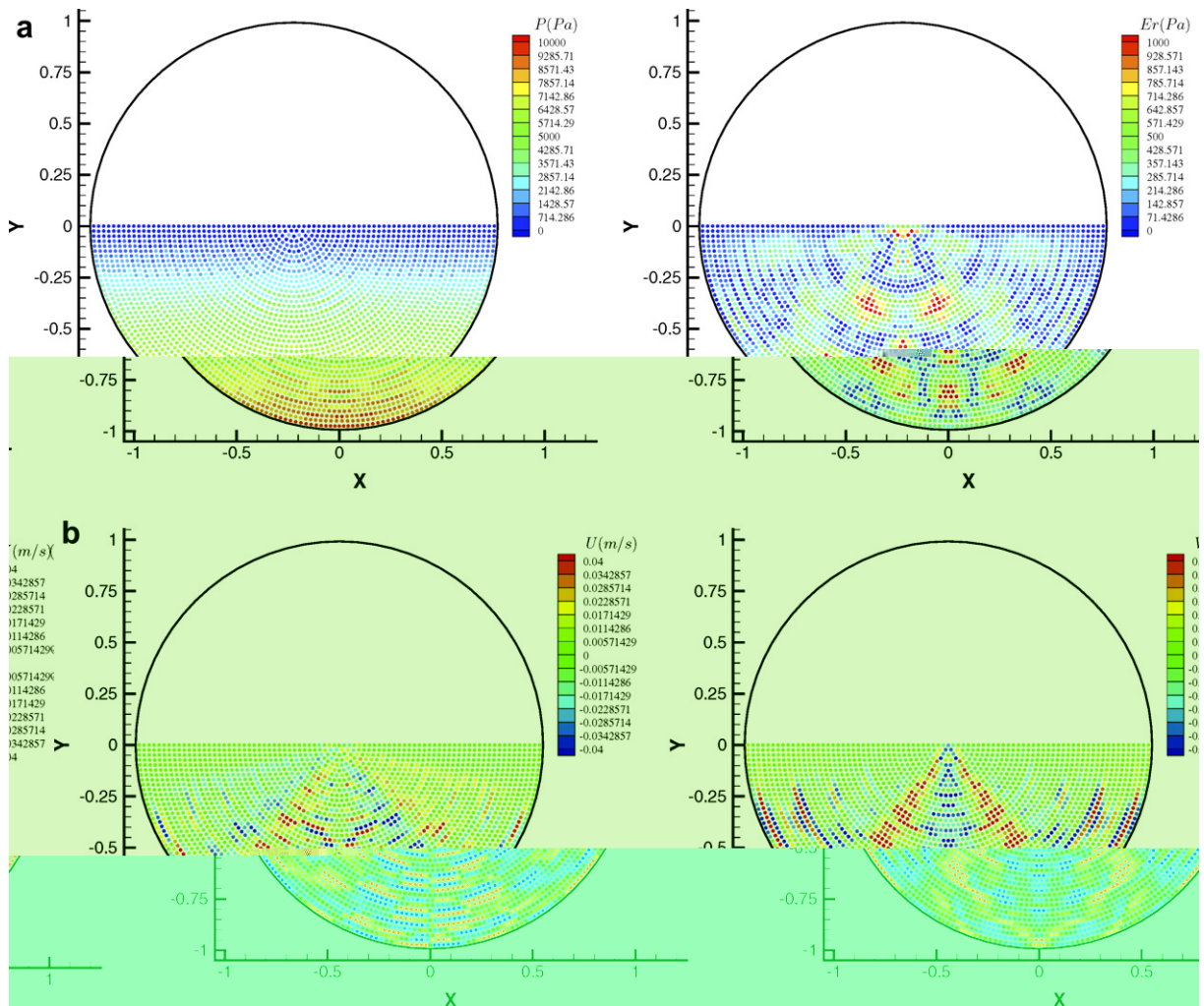

Fig. 10. Renormalized SPH scheme results. (a) Pressure (left) and error $\text{Er} = |P_{\text{SPH}} - P_{\text{exact}}|$ (right). (b) Horizontal (left) and vertical (right) velocity.

$$\frac{\partial P}{\partial y} = \frac{\partial P}{\partial \rho}\frac{\partial \rho}{\partial y} = -g\rho(y),$$

$$P(\rho) = \frac{\rho_0 c_0^2}{\gamma}\left[\left(\frac{\rho}{\rho_0}\right)^{\gamma} - 1\right].$$

After integration, and for $\rho = \rho_0$ at $y = 0$, the following initial conditions are obtained:

$$\vec{v}(x, y, t) = \vec{0},$$

$$P(x, y, t) = \frac{\rho_0 c_0^2}{\gamma}\left[\left(1 - \frac{(\gamma - 1)gy}{c_0^2}\right)^{\frac{\gamma}{\gamma-1}} - 1\right],$$

which is also the solution of this hydrostatic problem. This solution is compared to those of the renormalized non-coherent and the hybrid Taylor-SPH scheme results at the instant $t = 0.1$ s. The nominal speed of sound used is $c_0 = 80$ m/s and no artificial viscosity is implemented.
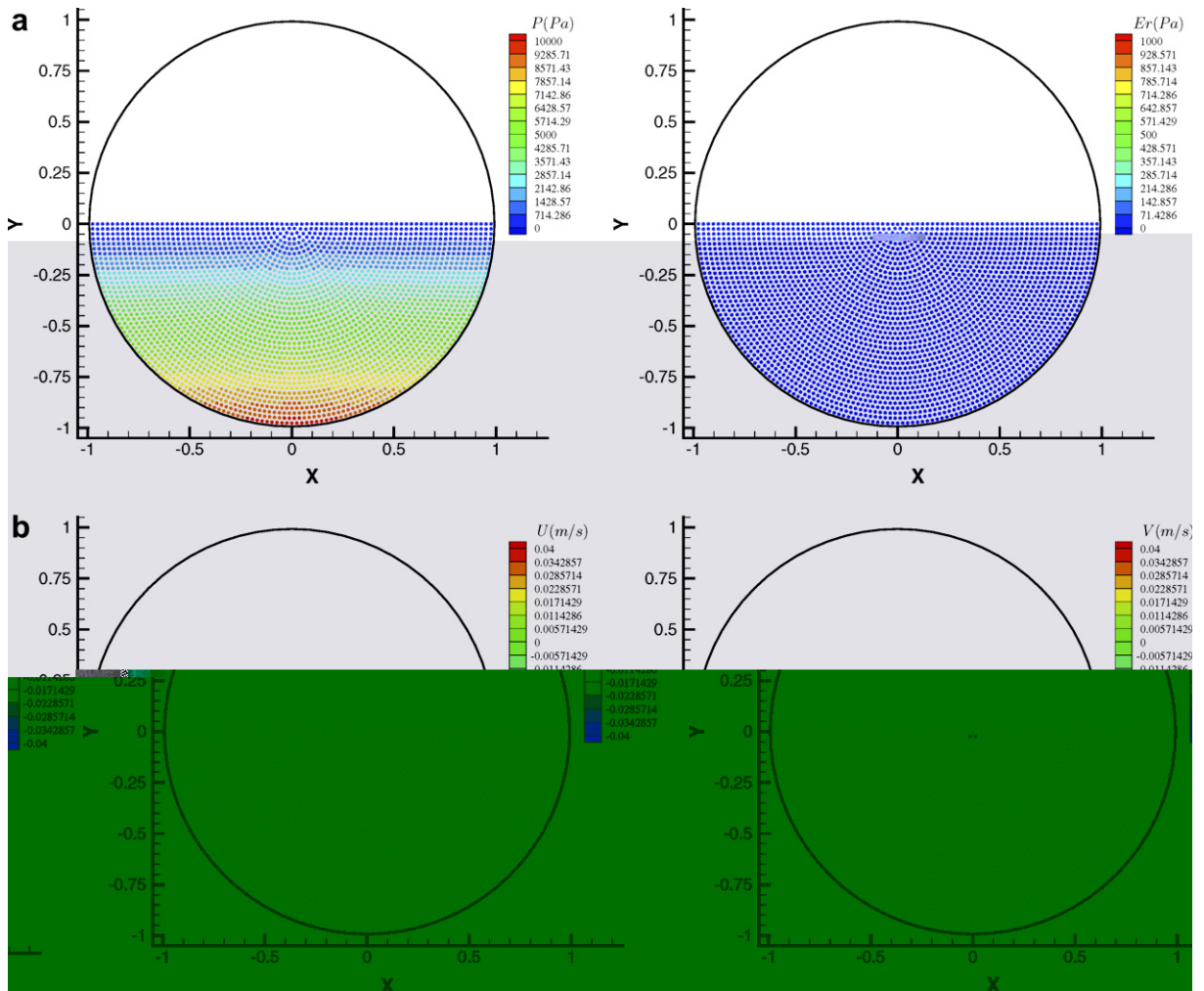

Fig. 11. Hybrid Taylor-SPH scheme results. (a) Pressure (left) and error $\text{Er} = |P_{\text{SPH}} - P_{\text{exact}}|$ (right). (b) Horizontal (left) and vertical (right) velocity.

7.1. Compressible hydrostatic results using the renormalized non-coherent scheme

As observed in the previous test case, the pressure and velocity results obtained with this formulation are heterogeneous and display strong errors (50–100% for the pressure), as shown in Fig. 10. The standard SPH solution is not provided since it gives similar results.

7.2. Compressible hydrostatic results using the hybrid Taylor-SPH scheme

Once again, this formulation yields more accurate and regular fields (Fig. 11). This confirms that the use of the renormalized non-coherent scheme at the free surface and the Taylor-SPH scheme elsewhere is indeed a viable method. The main errors observed (maximum 10% for the pressure) are due to uncertainties in the imposition of the dynamic free surface condition present in the renormalized non-coherent scheme.
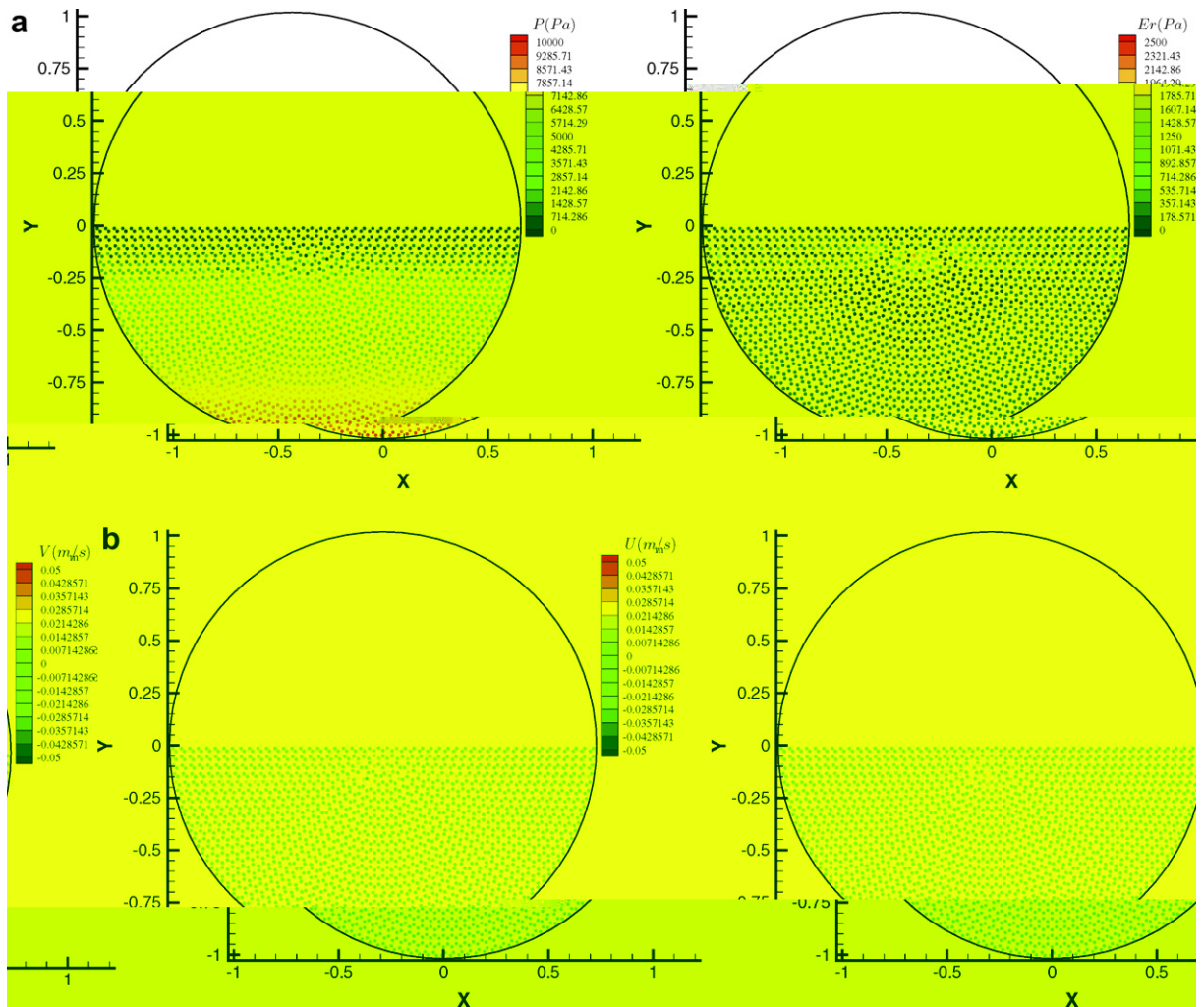

Fig. 12. Hybrid Taylor-SPH scheme results on an unstructured grid. (a) Pressure (left) and error $Er = |P_{SPH} - P_{exact}|$ (right) results. (b) Horizontal (left) and vertical (right) velocity results.

7.3. Compressible hydrostatic results using the hybrid Taylor-SPH scheme with a strongly unstructured particle grid

Fig. 12 refers to this free surface problem repeated on the unstructured grid of Fig. 7. Here again, these results are of sufficient quality to allow the use of a grid engine for the initial particle setting. This is despite the presence of larger errors in the free surface area (maximum 50% for the pressure) than elsewhere.

8. Stability study

For dynamic applications, all the formulations need to be stabilized using artificial viscosity [12,13,16]

$$
\Pi_{ij} = \begin{cases} -\alpha \frac{h \bar{c}_{ij}}{\bar{\rho}_{ij}} \frac{\vec{v}_{ij} \cdot \vec{r}_{ij}}{r_{ij}^2 + \epsilon h^2}, & \text{if } \vec{v}_{ij} \cdot \vec{r}_{ij} < 0, \\ 0, & \text{else}, \end{cases} \tag{35}
$$

where any value $\bar{f}_{ij}$ denotes $\frac{f_i + f_j}{2}$ and the equalities $\vec{v}_{ij} = \vec{v}_i - \vec{v}_j$, $\vec{r}_{ij} = \vec{x}_i - \vec{x}_j$ and $\epsilon = 0.01$ are adopted. Moreover c, h and α represent the speed of sound, the smoothing length and a non-dimensional amplitude parameter, respectively.

In this paper, for all formulations used, Π_{ij} is added to the pressure term within the momentum equation. For example, the Taylor-SPH scheme would become

$$
\begin{aligned}
\frac{d\rho_i}{dt} &= \rho_i \sum_j \frac{m_j}{\rho_j} (\vec{v}_i - \vec{v}_j) L(\vec{x}_i) \nabla W(\vec{x}_i - \vec{x}_j), \\
\frac{d\vec{v}_i}{dt} &= \vec{g} - \sum_j m_j \left(\frac{-P_i + P_j}{\rho_i \rho_j} + \Pi_{ij} \right) L(\vec{x}_i) \nabla W(\vec{x}_i - \vec{x}_j).
\end{aligned} \tag{36}
$$

Note that the increase in accuracy seen in this new formulation results in enhanced stability properties. This can be seen in the test case of a 2D weightless patch of fluid that is initially square in shape, and subjected to the following velocity field:

$$
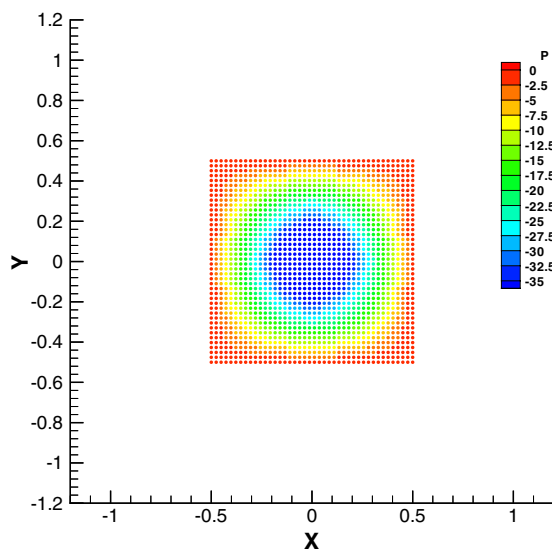\vec{v}(x, y, t = 0) = \begin{pmatrix} \omega y \\ -\omega x \end{pmatrix}, \tag{37}
$$

Fig. 13. Initial pressure field for $\omega = 5$ rad/s and $\rho = 1000$ kg/m³.

where ω denotes an arbitrary angular velocity. The initial pressure field is taken as the incompressible solution of the Poisson equation [17], that is

$$P(x, y, t = 0) = \rho \sum_{m=0}^{\infty} \sum_{n=0}^{\infty} \frac{-32\omega^2}{(mn\pi^2)\left[\left(\frac{n\pi}{L}\right)^2 + \left(\frac{m\pi}{L}\right)^2\right]} \cos\left(\frac{m\pi x}{L}\right) \cos\left(\frac{n\pi y}{L}\right).$$

This initial field is given in Fig. 13.

This challenging test case was first proposed and solved by Colagrossi [17] (see also Le Touzé and Colagrossi [18]). Due to centrifugal forces, the corners of this initial square are stretched and finally change into four fluid arms, while the square size decreases. This case results in large free boundary deformations, which are responsible for the occurrence of strong instabilities. The Lagrangian particle movements and the use of a
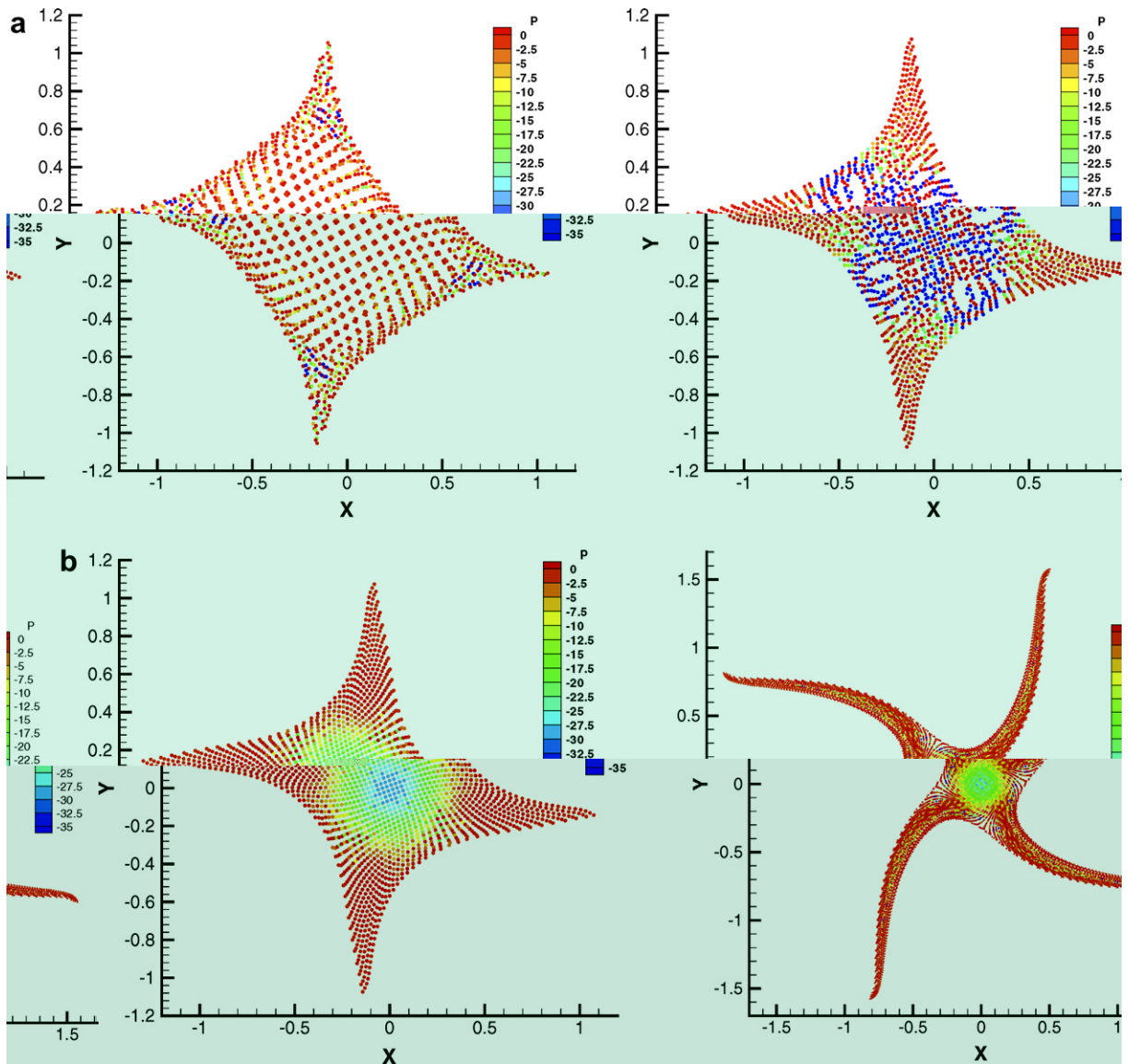

Fig. 14. SPH results on a rotating square patch of fluid. (a) Standard (left) and non-coherent renormalized (right) SPH scheme results (with $\frac{h}{\Delta x} = 1.23$) at $t = 2.45$ s. (b) Hybrid Taylor-SPH scheme results; left: $\frac{h}{\Delta x} = 1.23$ and $t = 2.45$ s; right: $\frac{h}{\Delta x} = 3$ and $t = 4.9$ s.

Cartesian grid as an initial particle setting result in the occurrence of line structures or particle clumpings. These progressively degrade the interpolation procedure, contaminating the entire simulation. Thus a highly accurate and stable scheme is required.

Figs. 14(a)(left and right) and (b)(left) show the results at $t = 2.45$ s, which allows enough time for the development of strong instabilities. In these simulations, the artificial viscosity coefficient used is $\alpha = 0.01$, and around 20 quadrature points are involved for each particle $\left(\frac{h}{\Delta x} = 1.23\right)$.

As observed in Fig. 14(a)(left), the standard SPH scheme for this test case causes the particles to clump into groups of four. These groups become isolated, preventing particles from interacting in sufficient numbers. The inaccuracies of this scheme appear to be responsible for this behavior. Note that the artificial viscosity does not help in any way in this problem, since this clumping occurs whatever the value of α is. This particle clumping is often attributed to the so-called "tensile instability" [19,20], for which Monaghan proposed an additional empiric term for the momentum equation [21]. This prevents particle clumping, but unfortunately induces chaotic pressure and velocity distributions. This study does not use a tensile instability control term.

As observed in Fig. 14(a)(right), the increase in accuracy due to renormalization helps to prevent particle clumping in this non-coherent scheme, but results in numerical fractures that contaminate the simulation. These fractures appear to be due to the inaccurate pressure gradient interpolation.

Fig. 14(b)(left) shows that the accuracy of the hybrid Taylor-SPH scheme prevents any particle clumping or numerical fractures, leading to better results. This allows the simulation to be run long after other schemes failed.

Despite these advantages, some line structures still exist, especially at the junctions of fluid arms. This damages the interpolation accuracy in that region. The use of a disordered initial particle setting would prevent the occurrence of these structures. However, this would degrade the gradient approximation quality in the free boundary area; the tips of the fluid arms being particularly sensitive. A costly but effective solution is to increase the ratio $\frac{h}{\Delta x}$. This limites the errors due to line structures, as illustrated in Fig. 14(b)(right).

9. Conclusion

Throughout this paper, accuracy aspects of the SPH method were considered. For this meshless method, accuracy is strongly connected to gradient approximations. The continuous equations convolute the desired field through a kernel gradient which systematically results in $O(h^2)$ convergence. However, the discrete forms of the equations do not yield such high accuracy. Simple convergence tests showed slow convergence for a disordered distribution of interpolation points. The convolution is approximated with a trapeze-like quadrature formula, which requires prohibitive particle numbers to obtain high order convergence. A general symmetric form of the Euler equation discretization, which respects the coherence and reciprocal interaction principles, was introduced. Among all the possibilities offered by this symmetric form, the only one without any $\nabla \rho$ terms was retained because of its direct match to the Taylor expansion. Within the momentum equation a term approximating the dynamic free surface condition was identified. This term was shown to justify the chosen form of the momentum equation discretization. The renormalization procedure and its relationship to the Taylor expansion was discussed, revealing a conflict between the momentum equation discretization and accuracy requirements. Additionally, it was shown that the coherence and the reciprocal interaction principles could be flouted, allowing the introduction of a new more accurate SPH formulation. As this formulation does not include a dynamic free surface condition approximation, it was first validated using a simple test case without a free boundary. Comparisons to the known analytical solution confirmed the accuracy of this new scheme, even for a strongly disordered particle grid. To extend this new formulation to free surface flow simulations, it was necessary to couple it with a non-coherent renormalized scheme for the free surface areas. This coupled scheme showed significant accuracy improvements when tested with a simple compressible hydrostatic test case. A stability study considered an initially square patch of fluid subjected to centrifugal forces. This resulted in impressive improvements by limiting any particle clumping and fracture effects. For this last test case, where the standard SPH method resulted in tensile instability, the new scheme overcame this undesirable effect without implementing any tensile instability control terms.

Acknowledgments

References

[1] J.J. Monaghan, Simulating free surface flows with SPH, Journal of Computational Physics 110 (1994) 399–406.

[2] G. Oger, M. Doring, P. Ferrant, B. Alessandrini, Two-dimensional SPH simulations of wedge water entries, Journal of Computational Physics 213 (2006) 803–822.

[3] K. Shintate, H. Sekine, Numerical simulation of hypervelocity impacts of a projectile on laminated composite plate targets by means of improved SPH method, Composites Part A: Applied Science and Manufacturing 35 (2004) 683–692.

[4] J. Bonet, S. Kulasegaram, M. Rodriguez-Paz, M. Profit, Variational formulation for the smooth particle hydrodynamics (SPH) simulation of fluid and solid problems, Computer Methods in Applied Mechanics Engineering 193 (2004) 1245–1256.

[5] L.D. Libersky, A.G. Petschek, T.C. Carney, J.R. Hipp, F.A. Allahdadi, High strain Lagrangian hydrodynamics: a three-dimensional SPH code for dynamic material response, Journal of Computational Physics 109 (1993) 67–75.

[6] J.P. Vila, A. Rompteaux, Calcul du tossage avec Smart Fluids un code de calcul particulaire compressible, in: Proceedings des 7emes Journées de l'Hydrodynamique, 1999.

[7] T. Belytschko, Y. Kongrauz, J. Dolbow, C. Gerlach, On the completeness of meshfree particle methods, International Journal of Numerical and Mechanical Engineering 43 (1998) 785–819.

[8] J. Bonet, T.S.L. Lok, Variational and momentum preservation aspects of smooth particle hydrodynamics formulations, Computer Methods in Applied Mechanics Engineering 180 (1999) 97–115.

[9] J.P. Vila, On particle weighted methods and SPH, Mathematical Models and Methods in Applied Sciences 9 (1999) 161–210.

[10] G.R. Johnson, S.R. Beissel, Normalized smoothing functions for impact computations, International Journal of Numerical Methods and Engineering 39 (1996) 2725–2741.

[11] R.W. Randles, L.D. Libersky, Smoothed particle hydrodynamics: Some recent improvements and applications, Computer Methods in Applied Mechanics Engineering 139 (1996) 375–408.

[12] J.J. Monaghan, Smoothed particle hydrodynamics, Annual Review of Astronomy and Astrophysics 30 (1992) 543–574.

[13] J.J. Monaghan, SPH and Riemann solvers, Journal of Computational Physics 136 (1997) 298–307.

[14] A. Colagrossi, M. Landrini, Numerical simulation of interfacial flows by smoothed particle hydrodynamics, Journal of Computational Physics 191 (2003) 448–475.

[15] M. Doring, Développement d'une méthode SPH pour les applications à surface libre en hydrodynamique, Ph.D. thesis, Ecole Centrale de Nantes, June 2005.

[16] J.P. Morris, J.J. Monaghan, A switch to reduce SPH viscosity, Journal of Computational Physics 136 (1997) 41–50.

[17] A. Colagrossi, A meshless Lagrangian method for free-surface and interface flows with fragmentation, Ph.D. thesis, Universita di Roma La Sapienza, 2005.

[18] D. LeTouzé, A. Colagrossi, Free-surface prototype problems suitable to investigate particle methods, in: Proceedings of the 20th International Workshop on Water Waves and Floating Bodies, 2005.

[19] J.W. Swegle, D.L. Hicks, S.W. Attaway, Smoothed particle hydrodynamics stability analysis, Journal of Computational Physics 116 (1995) 123–134.

[20] J.P. Morris, Analysis of smoothed particle hydrodynamics with applications, Ph.D. thesis, Department of Mathematics, Monash University, July 1996.

[21] J.J. Monaghan, SPH without a tensile instability, Journal of Computational Physics 159 (2000) 290–311.